Characteristics of Convectively Generated Gravity Waves Resolved by ERA5 Reanalysis

Hamid A. Pahlavan, John M. Wallace, and Qiang Fu

Department of Atmospheric Sciences, University of Washington, Seattle, Washington

ABSTRACT: ERA5 reanalysis with hourly time steps and 30 km horizontal resolution resolves a substantially larger fraction of the gravity wave spectrum than its predecessors. Based on a novel representation of the two-sided zonal wavenumber-frequency spectrum, we show evidence of gravity wave signatures with phase speeds centered around ±35 m s^{-1} in a suite of atmospheric fields. Cross-spectrum analysis reveals (i) a substantial upward flux of geopotential for both eastward and westward propagating waves, (ii) an upward flux of westerly momentum in eastward propagating waves and easterly momentum in westward propagating waves, and (iii) anticyclonic rotation of the wind vector with time— all characteristics of vertically propagating gravity and inertio-gravity waves. That two-sided meridional wavenumber-frequency spectra computed along individual meridians and then zonally averaged exhibit characteristics similar to the spectra computed on latitude circles indicates that these waves propagate in all directions. The three-dimensional structure of these waves is also documented in composites of the temperature field relative to grid-resolved, wave-induced downwelling events at individual reference grid points along the equator. It is shown that the waves radiate outward and upward relative to the respective reference grid points, and their amplitude decreases rapidly with time. Within the broad continuum of gravity wave phase speeds there are preferred values around ±49 m s^{-1} and ±23 m s^{-1}, the former associated with the first baroclinic mode in which the vertical velocity perturbations are of the same sign throughout the depth of the troposphere, and the latter with the second mode in which they are of opposing polarity in the lower and upper troposphere.

1. Introduction

Gravity waves with a wide range of space and time scales are clearly discernible in the vertical velocity, horizontal wind, geopotential, and temperature fields in today's high resolution global analyses. The upward transport of mechanical energy and momentum that they produce play an important role in the dynamics of the middle atmosphere, especially in the tropics (Fritts and Alexander 2003).

Gravity waves can be excited by a variety of mechanisms, including flow over topography, convection, shear instability, adjustment of unbalanced flow in the vicinity of jet streams and frontal systems, and wave-wave interactions (Fritts and Alexander 2003). The dissipation and breaking of convectively forced gravity waves have profound impacts on the dynamics of the tropical stratosphere. Together with planetary-scale Kelvin, mixed Rossby-gravity (MRG), and inertio-gravity (IG) waves, they are responsible for the descent of the alternating easterly and westerly wind regimes in the quasi-biennial oscillation (QBO) (Dunkerton 1997; Piani et al. 2000; Kawatani et al. 2010; Ern et al. 2014; Pahlavan et al. 2021a,b). They also contribute to modulating the tropopause temperature and the life cycle of cirrus clouds, both of which influence the water vapor transport to the stratosphere (Kim and Alexander 2015; Podglajen et al. 2016).

Our knowledge of gravity waves is limited because they tend to be intermittent and because motions on even smaller scales are involved in their generation, propagation, and dissipation (Alexander et al. 2010; Geller et al. 2013). Numerous observational and modeling studies have been aimed at improving our knowledge and understanding of the waves excited by convection (e.g., Alexander et al. 1995; Piani et al. 2000; Lane et al. 2001; Song et al. 2003; Alexander et al. 2004). However, many of these investigations are focused on a single convective event and/or on a single observation site. Aircraft and balloons have been used to extend the subsynoptic scale measurements over larger regions (e.g., Pautet et al. 2019; Rapp et al. 2021; Corcos et al. 2021), yet they can only provide local information on gravity wave characteristics. Satellite observations also reveal extensive wave structures (e.g., Alexander and Barnet 2007; Alexander and Ortland 2010; Ern et al. 2018; Wright et al. 2021), but they are limited with respect to their spatial and temporal coverage.

Despite the dramatic improvements in the computational power in the past decade, the spatial resolution of past general circulation models has been too coarse (i.e., ~100 km) to properly resolve the smaller scale gravity waves and to reveal their characteristics such as dissipation, interactions, spectral evolution, and source intermittency. Therefore, the effects of the unresolved gravity waves upon the global circulation are usually parameterized. These parametrization schemes, however, are oversimplified, leading to large uncertainties in the atmospheric circulation characteristics (e.g., Garcia et al. 2017). In particular, simulation of the QBO remains challenging (Richter et al. 2020a; Bushell et al. 2020; Butchart et al. 2020), and how the characteristics of the QBO might change in response to climate change is currently unclear. Although global simulations at kilometer-scale resolutions have become feasible very

Corresponding author: Hamid A. Pahlavan, pahlavan@uw.edu

recently, they are still limited to relatively short simulations. Furthermore, these simulations are not constrained by observations, and are therefore subject to undocumented systematic errors.

Numerical weather prediction (NWP) models and the associated reanalyses have just reached the resolution at which the larger scale gravity waves are being resolved (e.g., Preusse et al. 2014; Jewtoukoff et al. 2015; Podglajen et al. 2020). Representation of the waves is improving not only because of increasing model resolution, but also by advances in data assimilation techniques and by an expanding array of data that are being assimilated into the models. The gridded fields produced in the reanalyses are derived from high-resolution state-of-the-art NWP models constrained by decades of observations, and as such, they could serve to bridge the gap between the sparse, spectrally limited observations from satellites and field campaigns and the unconstrained, short simulations with high-resolution models.

Several studies have examined the realism of the small scale gravity waves in European Centre for Medium Range Forecasts (ECMWF) operational model (0.125° in the horizontal with 91 vertical levels) by comparing them with observations (Schroeder et al. 2009; Yamashita et al. 2010; Preusse et al. 2014; Jewtoukoff et al. 2015), and generally, have found them to be in good agreement. Here, we use ERA5, the newest reanalysis product of ECMWF's Integrated Forecast System (IFS) to investigate the characteristics of gravity waves. With a spatial horizontal resolution of 0.28° (~31 km), and 137 hybrid model levels with a top at 0.01 hPa, ERA5 resolves a significant fraction of gravity wave spectrum. The unprecedented hourly temporal resolution in ERA5 also makes it possible to resolve waves with periods as short as 2 hours.

Figure 1 provides an example of the resolved, convectively generated gravity waves in ERA5 over the tropics. The top panel is a visible image in the Pacific Ocean obtained by the Himawari-8 satellite, which shows several synoptic scale convective systems on August 7, 2015, at 0200 UTC. Fig. 1b shows the field of vertical velocity at the 50 hPa level (w_{50}) from ERA5 for the same time and region. The black contours denote the 250 K brightness temperature from Himawari-8 and are indicators of thick clouds with cold tops. The 50 hPa level is well above the top of these clouds, so the velocity perturbations at this level are produced mainly by vertically propagating gravity waves. It can clearly be seen that several concentric arrays of waves are radiating outward from the center of the convective systems, with the wave fronts wrapped in tight spirals: a pattern that is previously observed in satellite images, observations, and numerical simulations (e.g., Nolan and Zhang 2017). That the propagation is mostly eastward is expected, given that the zonal wind background was easterly, around -15 m s^{-1} at the 50 hPa level at that time. Figure 1c shows the standard deviation of the w_{50} field for the 24-hour period centered on 0200 UTC on this day. The enhanced variance around and to the right of the convective systems is clear and is indicative of enhanced wave activity. The purpose of this study is investigating the characteristics of these short-wavelength, high-frequency gravity waves. In this paper, we use the term inertio-gravity for referring to the low-frequency gravity waves for which the rotation of the Earth has an important influence (see Fig. 2).

Podglajen et al. (2020) investigated the gravity wave spectra in several of the reanalysis products using one-dimensional spectra in zonal wavenumber and frequency space. They found that on the whole, the reanalyses represent the spectral characteristics of the gravity waves quite realistically: notably the spectral gap between planetary waves and the smaller scale, higher frequency gravity waves. They also documented the intermittency properties of the gravity waves field and the shape of the probability density function of the fluctuations and showed them to be consistent with long-duration, quasi-Lagrangian balloon observations. Of the various reanalyses that they examined, they found that ERA5 to be the most realistic.

Gupta et al. (2021) used ERA5 to investigate the role of gravity waves during an Antarctic polar vortex breakdown. They showed that the resolved wave forcing in ERA5 accounts for as much as one-fourth of the observed wind deceleration during the period of the breakdown. In an intercomparison between five different reanalyses, they also showed that wave induced drag in ERA5 is by far the strongest.

Pahlavan et al. (2021a) investigated the dynamics and momentum budget of the QBO in ERA5. They showed that half the required QBO wave forcing is provided by resolved waves, approximately twice as much as in ERA-Interim, the previous reanalysis product from ECMWF (Dee et al. 2011), with horizontal resolution of 0.75° and 60 vertical levels. They also showed that this difference is mainly attributable to forcing from small-scale gravity waves with wavelengths shorter than 2000 km, which do not make an important contribution in ERA-Interim (their Fig. 14).

In all the reanalysis products, including ERA5 (and even in the models with resolutions much higher than ERA5), a significant part of the variability is still missing, especially at high frequencies and/or on short timescales, and hence needs to be parameterized. It has also been shown that waves in the reanalyses are not entirely self-generated by the models but derive in part from assimilated observations (Podglajen et al. 2020).

Here we further examine the representation of resolved gravity waves in the ERA5. Consistent with previous studies, we find that ERA5 is capable of resolving a significant part of the gravity wave spectrum with periods as short as 2 hours. Our results show that data from ERA5 can provide valuable information on gravity wave spectral characteristics, structure, and propagation, and thereby help to fill a

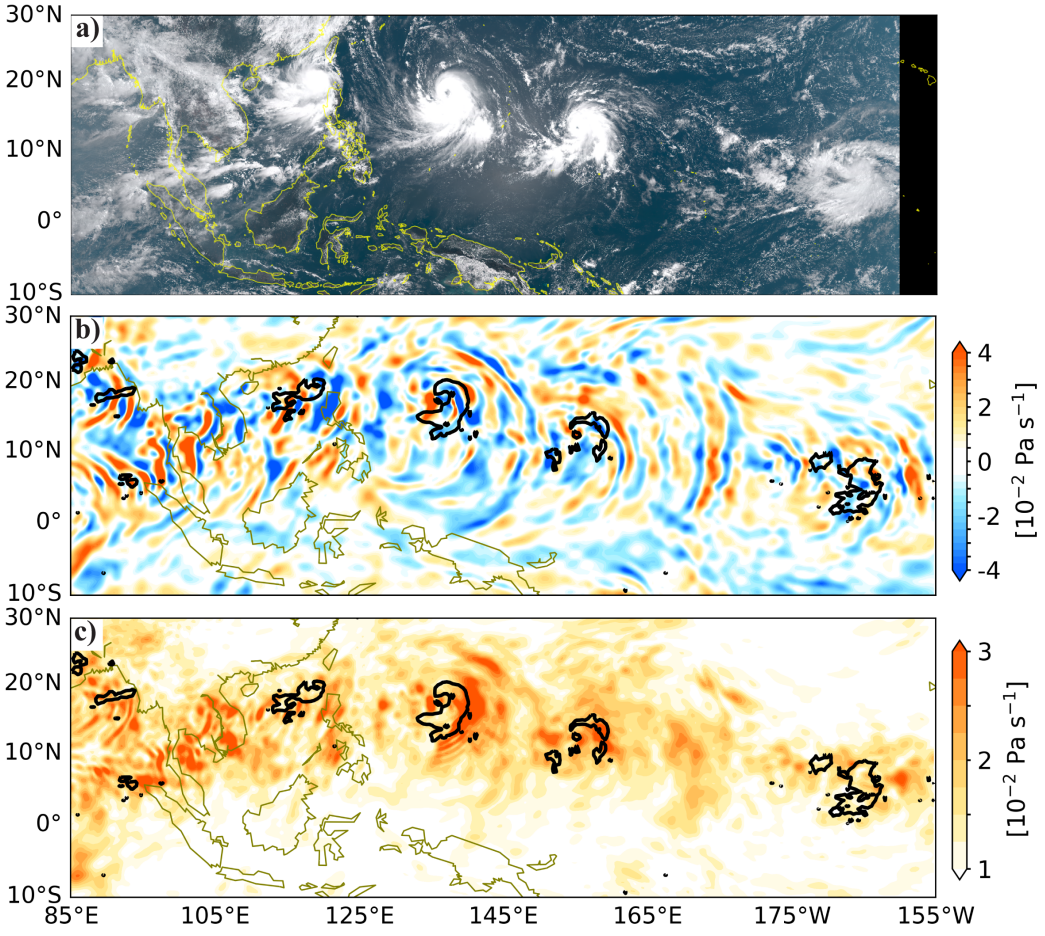

FIG. 1. (a) Visible imagery of the tropical Pacific Ocean from the Himawari-8 satellite on August 7, 2015, at 0200 UTC. (b) Vertical velocity at the 50 hPa level (w_{50}) from ERA5 for the same time and region (colored shading). (c) Standard deviation of the w_{50} field for the 24-hour period centered on 0200 UTC on this day (colored shading). The black contours in (b) and (c) denote the 250 K brightness temperature from Himawari-8 and are indicators of thick clouds with cold tops.

key knowledge gap that underlies the current deficiencies in weather and climate modeling.

In this study, we first introduce a novel representation of the two-sided zonal wavenumber frequency spectrum that is well suited for the study of tropical gravity waves. This representation is then used to examine the spectral characteristics of gravity waves in ERA5. We show that a suite of atmospheric fields exhibits clear gravity wave signatures extending along the broad swaths in the wavenumber-frequency domain with a broad range of phase speeds centered around ±35 m s-1. Cross-spectrum analyses between different variables also show characteristics consistent with those of vertically propagating gravity waves. The three-dimensional structure of these waves and their spatiotemporal evolution is further analyzed by means of compositing analysis. It is shown that the waves radiate outward and upward relative to their reference grid point. In both spectral and compositing analyses, there is evidence of two prevalent modes with phase speeds of 23 and 49 m s^{-1}, which correspond to the first and second baroclinic modes of the tropospheric diabatic heating (or vertical velocity) field.

A description of ERA5 reanalysis dataset and our methodology is given in Section 2, and we present and discuss the results in Section 3. Section 4 provides a further explanation of the two prevalent modes and discusses some of the compositing results in greater detail. A few concluding remarks are presented in Section 5.

2. Data and methodology

The ERA5 reanalysis data (Hersbach et al. 2020) is the 5th generation of ECMWF Reanalysis products, which is produced using the IFS cycle 41r2 with four-dimensional variational (4DVar) data assimilation. An artificial sponge layer is used in IFS to damp wave motions that propagate upward into the region near the model top (Shepherd et al.

2018). In comparison to its predecessor (ERA-Interim), ERA5 has 0.28° vs. 0.75° horizontal spacing between grid; 137 vs. 60 levels; and hourly vs. 6-hourly available data, allowing for a better representation of high frequency and/or small scale gravity waves that are known to be sensitive to resolution (Hoffmann et al. 2019; Hersbach et al. 2020). Furthermore, the use of an updated and significantly improved NWP model and data assimilation system compared to earlier reanalyses, along with the incorporation of data from additional sources, have improved the predictive skill of the forecast model used in producing ERA5, making it possible to use a smaller data assimilation increment (Hoffmann et al. 2019).

In this study, we retrieve ERA5 hourly data at 0.25° × 0.25° horizontal sampling on standard pressure levels. Most of the results shown in this paper are based on a 10-year period (2010-2019) of hourly data. We show examples confirming that very similar results are obtained when the same analyses are performed on 41 years of data (1979-2019).

Though the dynamical core can, in principle, resolve waves with a horizontal wavelength double the horizontal resolution, hyperdiffusion, which is introduced to provide numerical stability, limits the wavelengths of well-resolved waves to about 10 spatial grid points (Skamarock et al. 2014; Preusse et al. 2014). Considering the horizontal resolution of 31 km of ERA5 (639 spectral coefficients), waves with horizontal wavelengths longer than ~300 km (zonal wavenumber $k < 130$) should be fully resolved in ERA5 fields. Shorter waves are present, but they are suppressed in amplitude.

Many of the results presented in this paper are based on spectral analysis in which the variance of a variable $A(x,t)$ on a latitude circle, where x is the zonal coordinate and t is time, is transformed into a two-sided power spectrum $P_A(k,\omega)$, where k is zonal wavenumber and ω is frequency. The power spectrum is the product of the space-time discrete Fourier transform of the variable $F_A(k,\omega)$ with its complex conjugate $F_A(k,\omega)^*$:

$$P_A(k,\omega) = F_A(k,\omega)F_A(k,\omega)^* \tag{1}$$

The cross-spectrum between A and B is given by the product of the Fourier transform of A times the complex conjugate of the Fourier transform of B:

$$P_{AB}(k,\omega) = F_A(k,\omega)F_B(k,\omega)^* \tag{2}$$

The real part of P_{AB} is referred to as the cospectrum (Co) and the imaginary part is called the quadrature spectrum (Q). The sum of cospectral estimates over all wavenumbers and frequencies is equal to the covariance between A and B. One can think of the quadrature spectrum as the cospectrum between A, and 90° phase shifted B at each frequency and wavenumber.

To calculate the spectral power, a two-dimensional Fourier transform is applied to the hourly data for each latitude in the tropical region (30° S/N). The spectra are smoothed by subdividing the timeseries into segments with the length of 48 days, overlapping by 35 days, so that we use every time step in our spectral analysis more than once. The length of the segments (i.e., 48 days) is chosen such that waves with periods as long as 10 days to be well resolved. From each segment, a linear trend is removed, and the edges of the time series segments are tapered with the Hann window, which is equivalent to a weighted cosine. We average all spectra over latitude circles ranging from 30°S to 30°N at a 1° interval (i.e., 61 samples), after weighting each by the cosine of latitude to account for the reduction of the grid cell area away from the equator. The averaging over time segments and latitude circles smooths the spectrum, as opposed to using a running-mean filter to reduce the noise. A similar averaging procedure is employed for the cross-spectral analysis, after calculating the cross-spectrum on each latitude circle for each time segment.

3. Results

As background for the results presented in this section, Fig. 2a shows a dispersion diagram for a set of wave solutions to a system of dry shallow-water equations on an equatorial beta plane, linearized with respect to a resting basic state (Matsuno 1966). To span the wide range of frequencies and wavenumbers resolved by ERA5, we use logarithmic scales for both horizontal and vertical coordinates, which correspond to zonal wavenumber (k) and frequency (ω), respectively. The right side (positive k) corresponds to eastward propagating waves, and the left side (negative k) corresponds to westward propagating waves. The curves represent the spectral signatures of equatorial Kelvin waves, MRG waves and eastward and westward-propagating IG waves. The curves for the IG waves asymptote rather rapidly to the respective gravity wave curves at higher frequencies. It is evident that tropical waves with frequencies higher than 1 cycle per day and/or wavenumbers larger than 20 are predominantly gravity waves. Equatorial Rossby waves do not appear in this plot because their frequencies are less than 0.1 cycles per day. In this representation, nondispersive waves such as Kelvin and gravity waves, for which ω/k is constant, appear as straight lines with a slope of one decade increase of ω per decade increase of k. Differences in phase speed are reflected, not as differences in slope, but as vertical displacements of the phase speed line. The black curves in both Figs. 2a and 2b are scaled to an equivalent depth (h_e) of 54 m, which corresponds to a phase speed (c) of 23 m s^{-1} (i.e., $c = \sqrt{gh_e}$). The gray curves in Fig. 2b are scaled to a phase speed of 49 m s^{-1}. These phase speeds match the features in the spectra shown next.

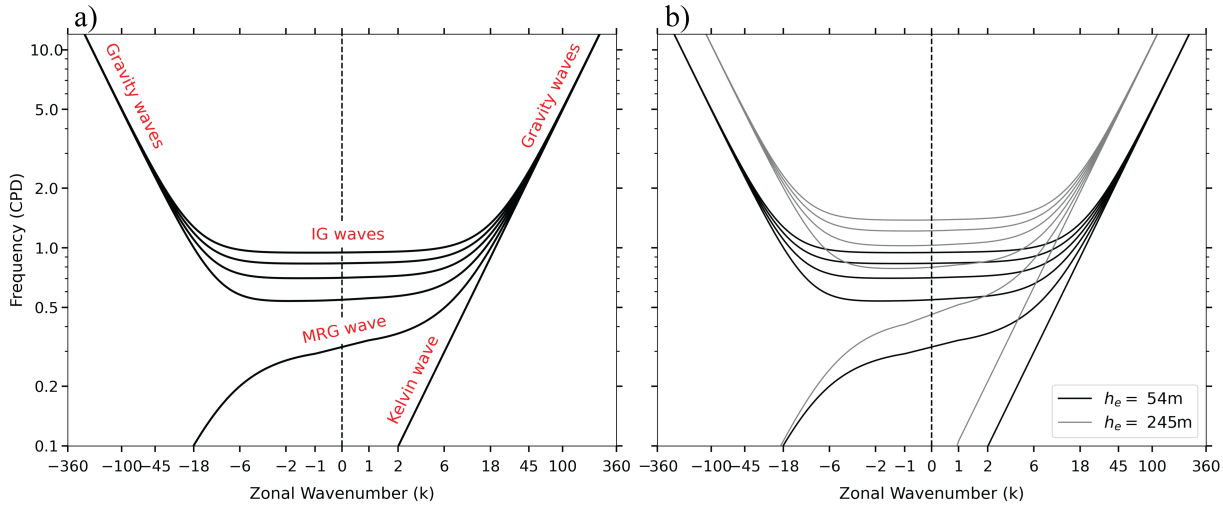

FIG. 2. (a) Dispersion diagram for a system of dry shallow-water equations on an equatorial beta plane, scaled to an equivalent depth (h_e) of 54 m to match a phase speed (c) of 23 m s^{-1} (i.e., $c = \sqrt{gh_e}$), plotted on logarithmic scales for both zonal wavenumber and frequency coordinates. The highest frequency in the spectra is 12 cycles per day (CPD), which is the Nyquist frequency (highest resolvable frequency) when hourly data is used. The zonal wavenumber is linear in the range k = -1 to 1. (b) The black curves are the same as in (a), but the gray curves are scaled to an equivalent depth of 245 m to match a phase speed of 49 m s^{-1}. Adapted from Matsuno (1966) with modifications.

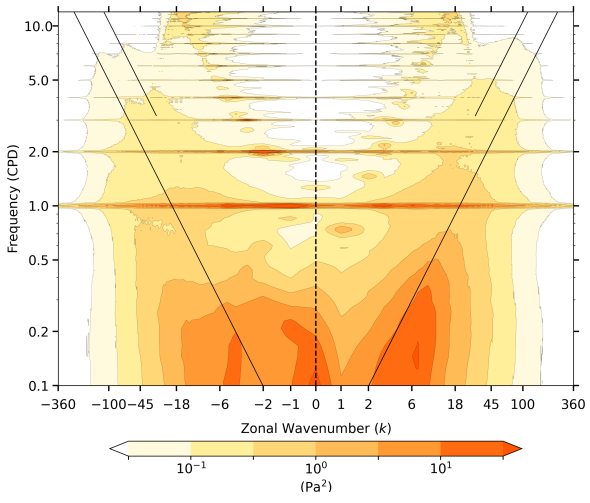

FIG. 3. Two-sided zonal wavenumber-frequency power spectrum for surface pressure on a logarithmic scale for wavenumber, frequency, and spectral density in unit of variance per unit area, from an average of 61 spectra computed at 1° latitude intervals between 30° S/N based on hourly data for 2010-2019. The spectral power is multiplied by $k \times \omega$ to preserve the property that (power × area) be proportional to variance anywhere on the plot. The contour interval corresponds roughly to a factor of 3. The sloping straight black lines correspond to phase speeds of ±49 m s^{-1} (upper) and ±23 m s^{-1} (lower). The scale of zonal wavenumber is linear from k = -1 to 1.

a. Spectral analysis

1) ZONAL WAVENUMBER-FREQUENCY SPECTRA

Figure 3 shows the power spectrum of surface pressure obtained by applying a two-dimensional Fourier transform to the hourly data on latitude circles between 30°S and 30°N at 1° intervals, a total of 61 samples, as explained in Section 2. A logarithmic scale is also used for indicating the spectral power (or density) in the observed spectrum, which spans several orders of magnitude (if a linear scale were used to represent it, most of the plot would be empty). The spectral power is multiplied by $k \times \omega$ to preserve the property that (power × area) be proportional to variance anywhere on the plot. Two lines of constant slope corresponding to the gravity waves with phase speeds of 23 and 49 m s^{-1} are plotted for reference. Note that all the spectra shown in this paper are raw spectra: they are not normalized with respect to a smooth background spectrum.

Figure 3 exhibits a "red" background spectrum in both ω and k, but with some distinctive features. The set of very thin horizontal bands centered on the diurnal period and its higher harmonics corresponds to the astronomically forced solar (24 h and its higher harmonics) and lunar (12.4 h) tides. Because of the geographically fixed boundary-forced component of the tides, peaks are observed on both sides of the spectrum, rather than only on the westward propagating side. The additional isolated peaks for each zonal wavenumber correspond to the external modes of the global atmosphere, which are extensively analyzed by Sakazaki and Hamilton (2020).

The focus of the present study is the internal gravity waves, which extend along the broad swaths in the wavenumber-frequency domain centered along 35 m s^{-1} for both eastward and westward propagating waves. The spectrum is continuous, but there is evidence of two preferred phase speeds, a faster one around ±49 m s^{-1}, and a slower one around ±23 m s^{-1}. We will show in Section 4

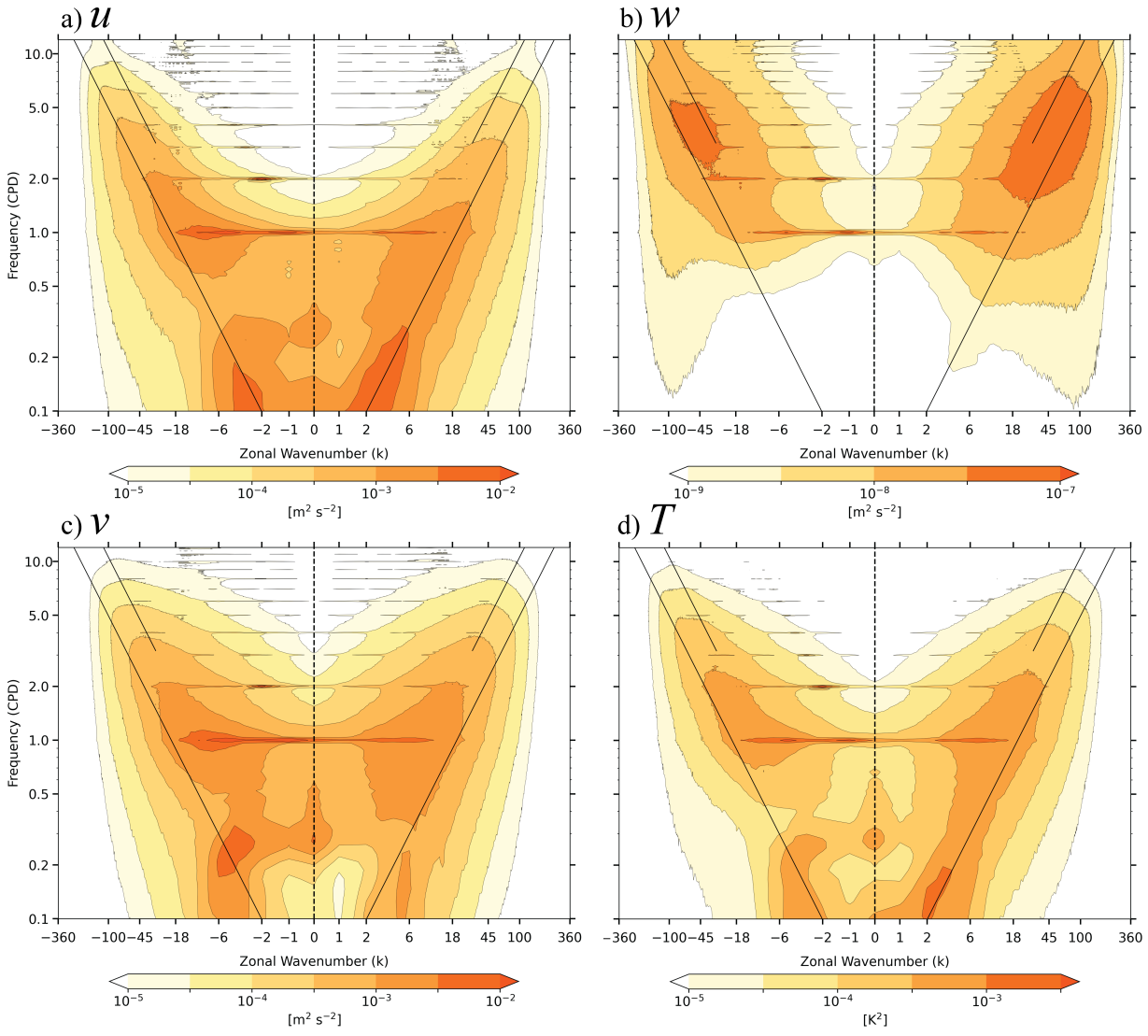

FIG. 4. Same as Fig. 3 but for (a) zonal wind, (b) vertical velocity, (c) meridional wind, and (d) temperature at the 50 hPa level.

that these correspond to internal waves with stratospheric vertical wavelengths of about 14 and 6.5 km, respectively.

The power spectrum of surface pressure is shown first because it is better constrained by observations than the other fields. While most radiosonde data are available only twice per day, ERA5 assimilates hourly observations of surface fields from 5000 aviation meteorology support (METAR) stations throughout the world as well as surface observations from another 10 000 synoptic meteorological (SYNOPS) stations that report four times per day or more frequently (Haiden et al. 2018).

Figure 4 shows the two-sided zonal wavenumber-frequency power spectra of zonal (u), meridional (v), and vertical (w) wind components, and temperature (T) at the 50 hPa level, constructed in the same manner as Fig. 3. The broad swaths related to the gravity waves are evident in all of them, including the evidence of two preferred phase speeds, the same as in Fig. 3. Most of the variance of the temperature and horizontal wind fields is concentrated in the low frequencies and small wavenumbers, whereas most of the variance of the vertical wind component is concentrated at higher frequencies. Equivalently, it can be said that spectra of temperature and horizontal winds are red, whereas the spectrum of vertical velocity is essentially white out to the limits of the spatial and temporal resolution of ERA5.

Figure S1 shows the two-sided zonal wavenumber-frequency power spectrum of vertical wind constructed using 41 years of data (1979-2019), and is very similar to Fig. 4b, which is based on 10 years of data (2010-2019).

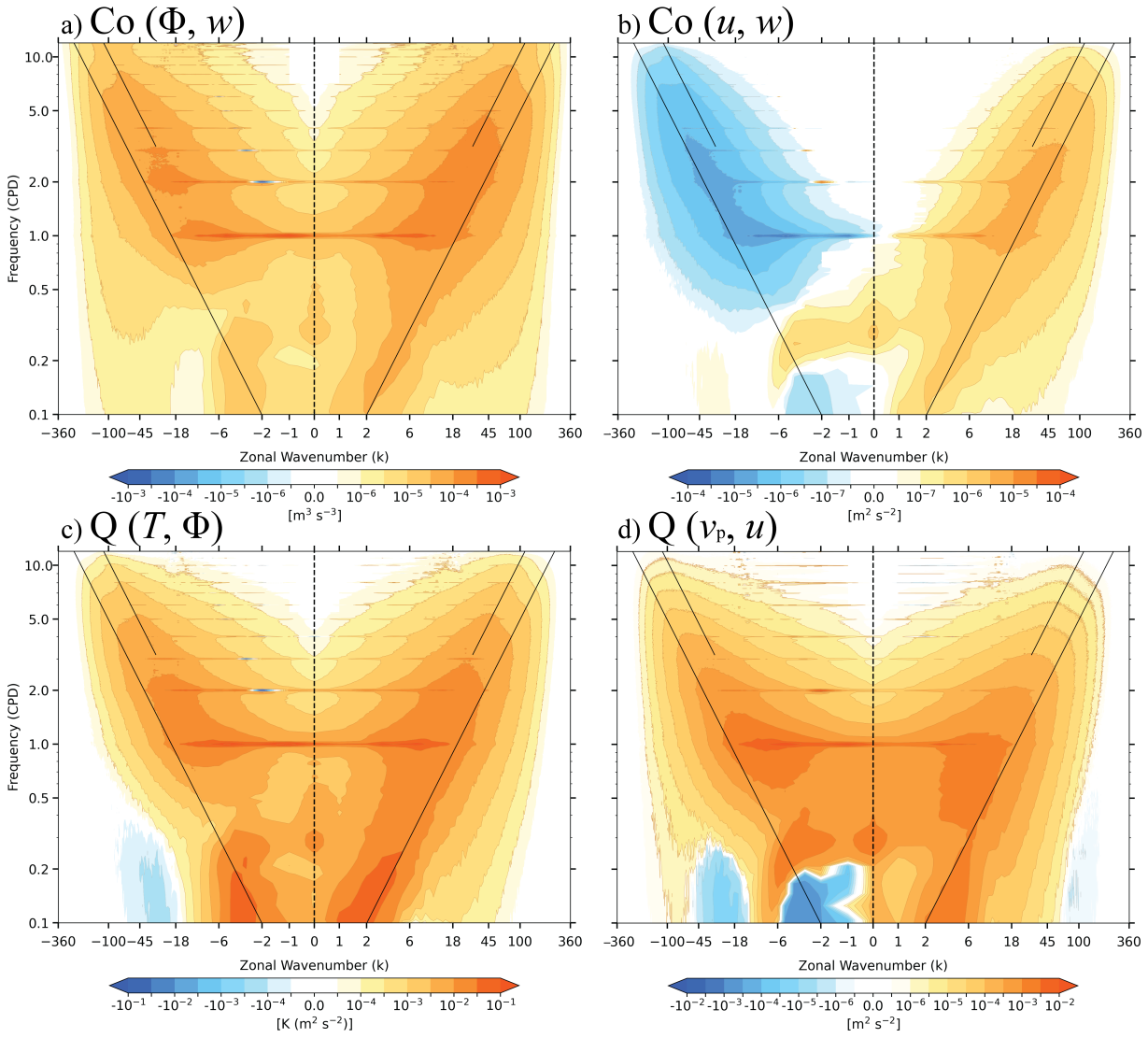

FIG. 5. Same as Fig. 3 but for the cospectrum (Co) between (a) geopotential and vertical velocity and (b) zonal wind and vertical velocity, and the quadrature spectrum (Q) between (c) temperature and geopotential and (d) poleward meridional (i.e., northward in the Northern Hemisphere and southward in the Sothern Hemisphere) and zonal components of the wind. All fields are at the 50 hPa level.

Hence, for the sake of computational efficiency, the shorter period has been used for performing analysis in this study.

It should be kept in mind that the signature of gravity waves in the spectra shown in Fig. 4 is, in effect, filtered by the mean background zonal wind, which is slightly easterly in the tropics. Accordingly, there is an asymmetry in the spectra with respect to k =0 with eastward propagating gravity waves having slightly larger amplitudes– most clearly evident in the power spectrum of vertical velocity. Due to the easterly background flow, eastward propagating gravity waves are Doppler-shifted toward higher intrinsic phase speeds, refracted to larger vertical wavelengths, and hence can attain larger amplitudes (Lane et al. 2001).

The background flow in the stratosphere is often varying on a time scale much longer than the period of the gravity waves, and hence, the linear theory is useful for describing the spectral characteristics of the waves in the stratosphere (Fritts and Alexander 2003). In the troposphere the separation between time scales is not as clean and the presence of convection and turbulence makes it more difficult to separate the gravity waves from the noisy background.

To evaluate the consistency of the observed spectra with linear gravity wave theory, we examine the relations between different variables. Cross-spectra for the three wind components, temperature, and geopotential (Φ) at the 50 hPa level are shown in Fig. 5. The cospectrum between w and Φ, an indicator of the vertical flux of geopotential and

mechanical energy, is shown in Fig. 5a. It is upward for both eastward and westward propagating waves, consistent with theory. The upward flux of zonal momentum (Fig. 5b) is positive for eastward propagating waves and negative for westward propagating waves, also consistent with theory. The quadrature spectrum between T and Φ (Fig. 5c), is much stronger than the corresponding cospectrum (Fig. S2), with T leading Φ, indicative of downward phase propagation. These relationships are characteristic of internal gravity waves. In external gravity waves the variations in Φ and T are in phase, rather than in quadrature.

In the quadrature spectrum between the poleward meridional (v_p, which is equal to v in the Northern Hemisphere and $-v$ in the Sothern Hemisphere) and zonal components of the wind (Fig. 5d), v_p leads u for both eastward and westward propagating waves, indicative of clockwise rotating trajectories in the Northern Hemisphere and counterclockwise rotating trajectories in the Southern Hemisphere—i.e., an anticyclonic turning of the wind with time in their respective hemispheres, consistent with the structure of IG waves. The dominance of anticyclonic rotation of the wind vectors is indicative of the dominance of linear IG waves as opposed to stratified turbulence, for which no systematic phase relation between the horizontal wind components is expected. The relationships between other variables not shown here are also consistent with the structure of vertically propagating gravity waves. For example, temperature is in quadrature with vertical velocity, while in quasi-geostrophic turbulence they should be either in phase or 180° out of the phase. That about half the vertical fluxes of zonal momentum shown in Fig. 5b is attributable to fluctuations with zonal wavenumbers greater than 20 and periods shorter than two days also attests to the importance of gravity waves in the general circulation of the tropical stratosphere.

Another notable feature in Fig. 5 is the MRG wave, which is evident in all the plots, in particular in Fig. 5b, where it transports westerly momentum upward. However, as explained in Holton (1973), the mean meridional circulation associated with MRG waves leads to a net upward transfer of easterly absolute angular momentum. Evidence of this transport can be seen in Fig. 13 of Pahlavan et al. (2021b). The blue patches at frequencies less than 0.2 cpd and wavenumbers k= -1 to-6 in Figs. 5b and 5d are related to extratropical Rossby waves, which propagate into the tropical stratosphere from the winter hemisphere. Another low-frequency blue patch is discernible in Figs. 5c and 5d at wavenumbers $k \approx$ -18 to -45. This signal does not seem to be related to baroclinic waves from midlatitudes, because it is apparent only in the easterly phase of the QBO, which will be discussed in the companion paper.

2) MERIDIONAL WAVENUMBER-FREQUENCY SPECTRA

In contrast to equatorially-trapped planetary-scale waves, which propagate only zonally, small-scale, high-frequency gravity waves should have no preferred direction of propagation. They are expected to propagate radially away from their sources, as seen in Fig. 1, and consequently, to exhibit similar spectral characteristics along any arbitrarily chosen direction. To test this expectation, we repeated our spectral analysis, this time performing a two-dimensional Fourier transform along each meridian from 30°S to 30°N at 2° zonal intervals (i.e., along 180 meridians).

The results are shown in Figs. 6 and 7. Here the horizontal coordinate is a function of meridional wavenumber (l), as opposed to the zonal wavenumber in the previous plots, and the right side (positive l) represents southward propagating, and the left side (negative l) represents northward propagating waves. Because only a 60° span of latitude is used in computing the spectra, meridional wavenumber 3 is the longest wave that can be sampled. It should also be noted that meridional wavenumber 180 has the same horizontal scale as a zonal wavenumber 360: they both are representative of waves with a wavelength of 1 degree.

The two-sided meridional wavenumber-frequency power spectra presented in Fig.6 exhibit the same characteristics as those shown in Fig. 4, including the same two preferred phase speeds, confirming that these waves propagate in all directions, as expected. For all variables, the spectra are almost perfectly symmetric about $l = 0$, due to the absence of a strong background meridional wind. It follows that their net wave forcing on the background meridional flow should be zero.

Figure 7 shows the relations between the different variables along the meridional direction. They are consistent with the structure of vertically propagating gravity waves, and analogous to those in the Fig. 5. They are also indicative of an upward flux of geopotential, downward phase propagation, and an anticyclonic turning of the horizontal wind vector with time. The vertical flux of meridional momentum (Fig. 7b) is indicative of an upward flux of southward momentum by southward propagating waves and an upward flux of northward momentum by northward propagating waves.

In this rotated frame of reference, the shape of the power spectrum of meridional wind in Fig. 6c, is analogous to that of zonal wind in the conventional frame of reference (Fig. 4a) and vice versa. Hence, to compare the two it is useful to refer to the wind components parallel to and perpendicular to the axis used in defining the wavenumber coordinate. In both Fig. 4 and Fig. 6, at frequencies higher than 1 cpd the preference for phase speeds higher than 49 m s^{-1} is stronger in the component perpendicular to the axis than in the component parallel to the axis. This feature is best illustrated in Fig. 8, which shows the

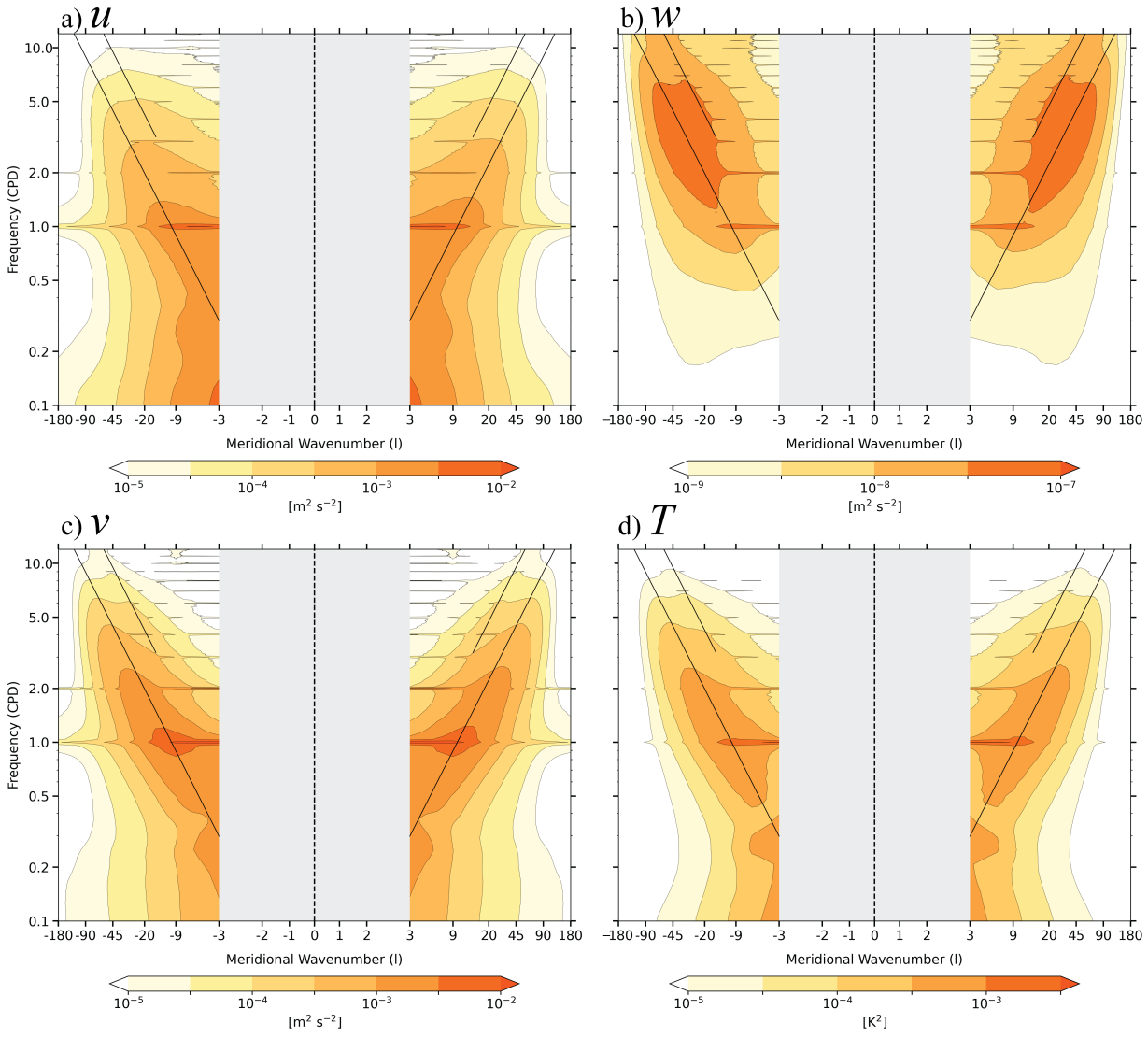

FIG. 6. Two-sided meridional wavenumber-frequency spectrum for (a) zonal wind, (b) vertical velocity, (c) meridional wind, and (d) temperature at the 50 hPa level. It is constructed in the same manner as Fig. 4, but the two-dimensional Fourier transform is applied along each meridian from 30°S to 30°N at 2° zonal intervals (i.e., along 180 meridians). Because only a 60° span of latitude is used in computing the spectra, meridional wavenumber 3 is the longest wave that can be sampled. The sloping straight black lines correspond to phase speeds of ±49 m s^{-1} (upper) and ±23 m s^{-1} (lower). The scale of meridional wavenumber is linear from l = -1 to 1.

ratio of the spectra of the horizontal winds in both conventional and rotated frames of reference. The blue regions inside the area confined with the ±49 m s^{-1} phase speed lines indicate the stronger power in the wind component perpendicular to the axis. This pattern suggests that the high frequency (i.e., higher than 1 cpd) gravity waves tend to be meridionally elongated in the zonal wind field and zonally elongated in the meridional wind field. An explanation of this pronounced anisotropy is beyond the scope of the present study because it may require consideration of turbulence as well as gravity waves.

The spectra along latitude circles (Fig. 8a) exhibits a distinctive MRG wave signature in which the meridional wind component is dominant along the dispersion curve, as indicated by the blue arch. There is no trace of this feature in the spectra along meridians (Fig. 8b).

b. Compositing analysis

Here we investigate and characterize the three-dimensional structure of the small-scale gravity waves by compositing different variables based on time series of tropospheric vertical velocity at individual reference grid points. The left panels in Fig. 9 show maps of tropospheric

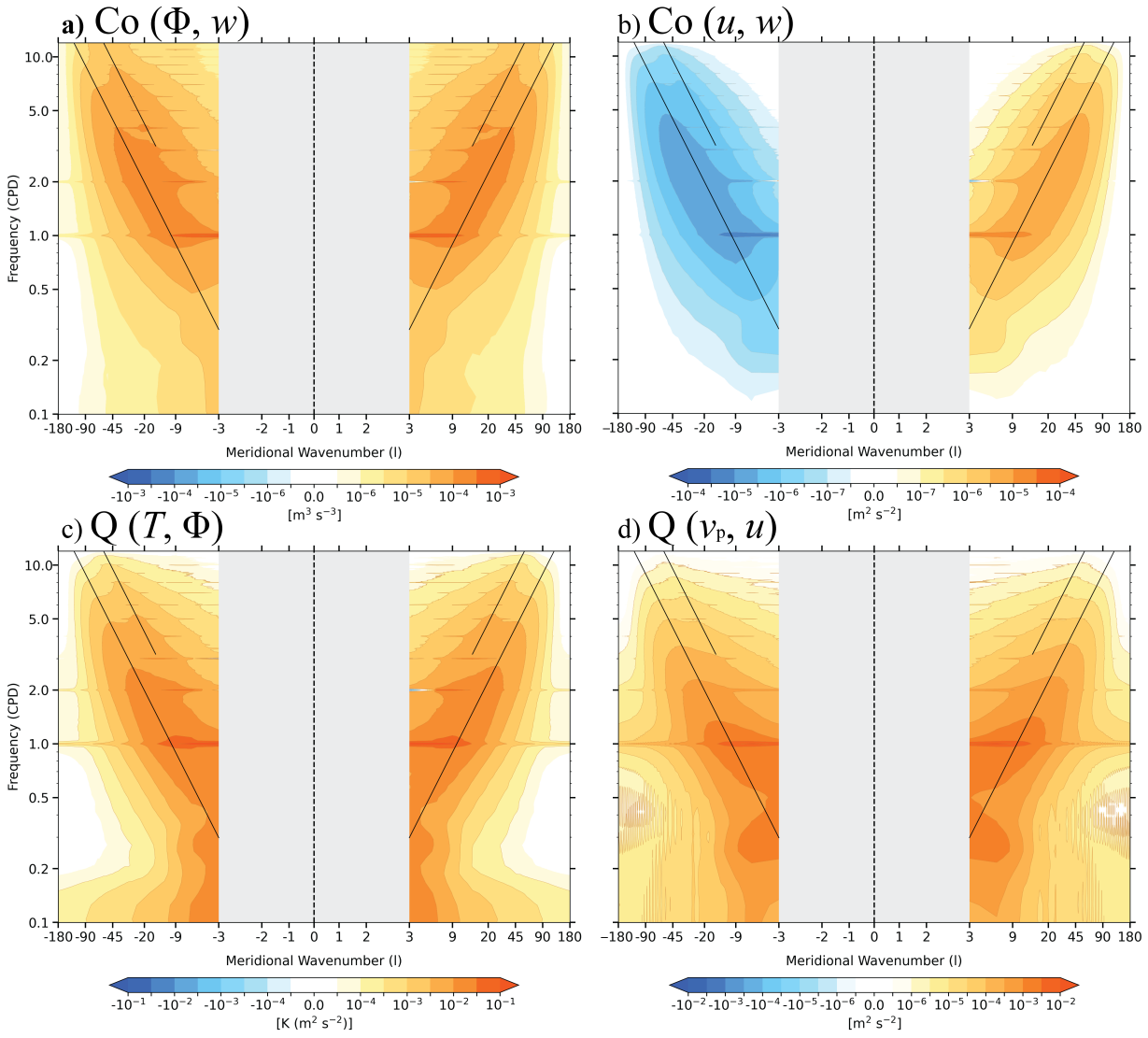

FIG. 7. Same as Fig. 6 but for the cospectrum (Co) between (a) geopotential and vertical velocity and (b) zonal wind and vertical velocity, and the quadrature spectrum (Q) between (c) geopotential and temperature and (d) poleward meridional and zonal components of the wind. All fields are at the 50 hPa level.

temperature, represented by 1000-200 hPa thickness, composited based on wave-induced downwelling events, as defined by the sum of the 700 and 300 hPa (geometric) vertical velocities (w_{300} and w_{700}) along a line of reference grid points, equally spaced along the equator at 1-degree intervals. Averaging w_{300} and w_{700} arguably yields a time series that closely resembles the principal component of the leading mode of variability of the vertical profile of vertical velocity in the tropics. To qualify as a downwelling event, an hourly observation of vertical velocity must lie in the bottom 10% of its frequency distribution at that grid point. The analysis is based on 10 years of hourly data. Hence, at each of the 360 grid points there are (365 × 24) events, yielding a total of roughly 3 million downwelling events. Many of them are overlapping and not entirely independent, but given the weakness of the temporal correlation in the vertical velocity values at individual grid points, which drops below ~0.4 at two hours, and the weak correlation between the vertical velocity time series a degree of longitude apart along the equator (also ~0.4), the number of statistical degrees of freedom in these composites cannot be much less than a million.

The right panels of Fig. 9 are different from the left panels in two respects: they show the upper tropospheric temperature, represented by the 500-200 hPa thickness, and they are based on $w_{300} - w_{700}$, which resembles the second principal component of the vertical velocity profile. The fields shown in the left column thus correspond to relatively

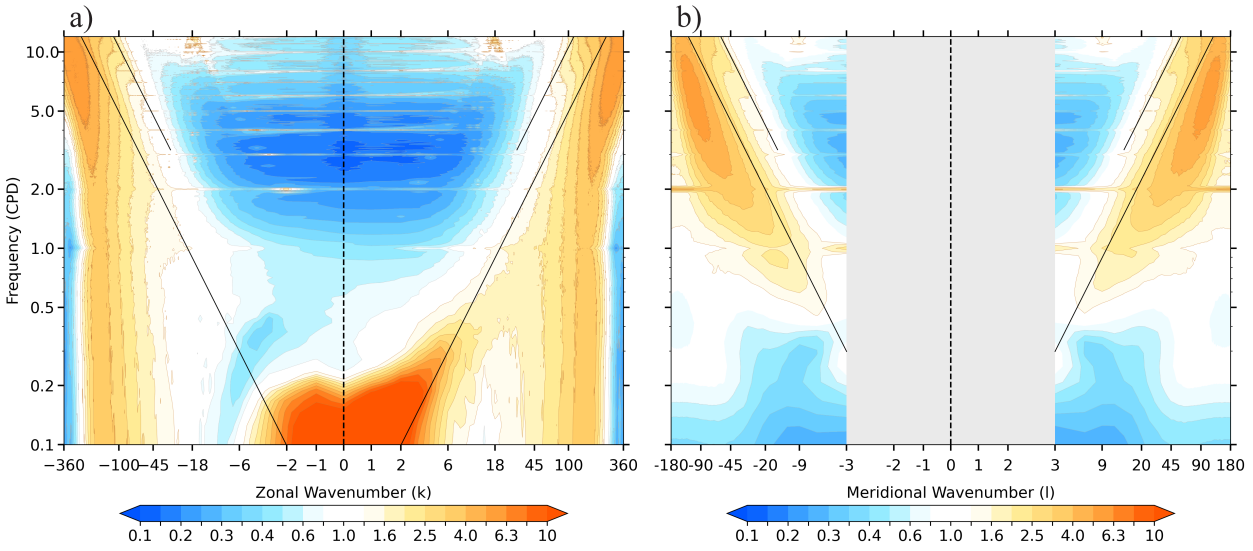

FIG. 8. (a) Two-sided zonal wavenumber-frequency spectrum for the ratio of zonal wind power spectrum to the meridional wind power spectrum (i.e., $P_u(k,\omega)/P_v(k,\omega)$) in a logarithmic scale. (b) Two-sided meridional wavenumber-frequency spectrum for the ratio of meridional wind to zonal wind power spectra (i.e., $P_v(l,\omega)/P_u(l,\omega)$).

deep waves in which vertical velocity perturbations of the same polarity extends through the depth of the troposphere, whereas those in the right panel correspond to shallower waves that undergo a phase reversal in the mid-troposphere.

The mean for each hour of the day has been removed from the geopotential height field (Z) in order to suppress the tidal signal. The data have been also high-pass filtered [1] in order to isolate the signature of high frequency gravity waves, which is much weaker than the temperature variability on longer time scales. Similar results can be obtained by performing principal component analysis (PCA) on the vertical velocity profiles and regressing the temperature field upon the expansion coefficients of the first and second modes.

These horizontal cross sections reveal an almost perfectly circularly symmetric structure at all levels. The waves appear to radiate outward from the reference grid point. The deeper wave propagates at about twice the rate of the shallower one, with a phase speed of ~50 versus ~25 m s^{-1}, consistent with the two preferred phase speeds seen in the spectra shown in the previous section. Further evidence of the prominence of these two modes, which are widely referred to in the literature as "the first and second baroclinic modes", respectively, is presented in Section 4.

The expanding rings are the signature of adiabatically-induced subsidence warming in downwelling gravity waves. The waves spread the latent heat injected into the atmosphere in convective updrafts into the large-scale environment, thereby imposing weak-temperature gradient (WTG) balance between the vertical velocity and diabatic heating fields throughout most of the tropical troposphere. That the temperature signal of the second mode is larger than that in the first mode (note the different color bars in Fig. 9) is consistent with previous studies and is due to the weaker cancellation between diabatic heating and adiabatic cooling in the second mode (Haertel and Kiladis 2004).

There exist numerous observations of gravity waves in the upper atmosphere, which are generated by convective sources and are often confirmed by their concentric or semi-concentric patterns in ground-based and satellite imagery (e.g., Miller et al. 2015). For example, Dewan et al. (1998) analyzed gravity waves in the satellite observations from the Midcourse Space Experiment. The density and temperature fluctuations, which were measured at ~40 km, showed wave fronts arrayed in concentric circles centered over a large thunderstorm. There are also numerous satellite images and videos from Hunga Tonga eruption on 15 January 2022, which show concentric internal and external waves radiating outward after the eruption. Furthermore, there are several modeling studies of the structure of convectively generated gravity waves in the Tropics that show wave fronts radiating out from centers of strong diabatic heating (e.g., Piani et al. 2000).

It should be emphasized that the patterns in our composites show the propagation of downwelling gravity waves, but they don't reveal the processes that generated them, which occur on scales much smaller than the ERA5 horizontal resolution of ~30 km. The patterns shown in Fig. 9 reveal the gravity waves that are present at the reference grid point at time zero and propagate away from it in the hours that follow. At negative lag times, gravity waves can

[1] The high-pass filtering has performed by applying a rolling window of 7-point binomial distribution (i.e., [-1, -6, -15, 44, -15, -6, -1]) to the timeseries at each individual grid point.

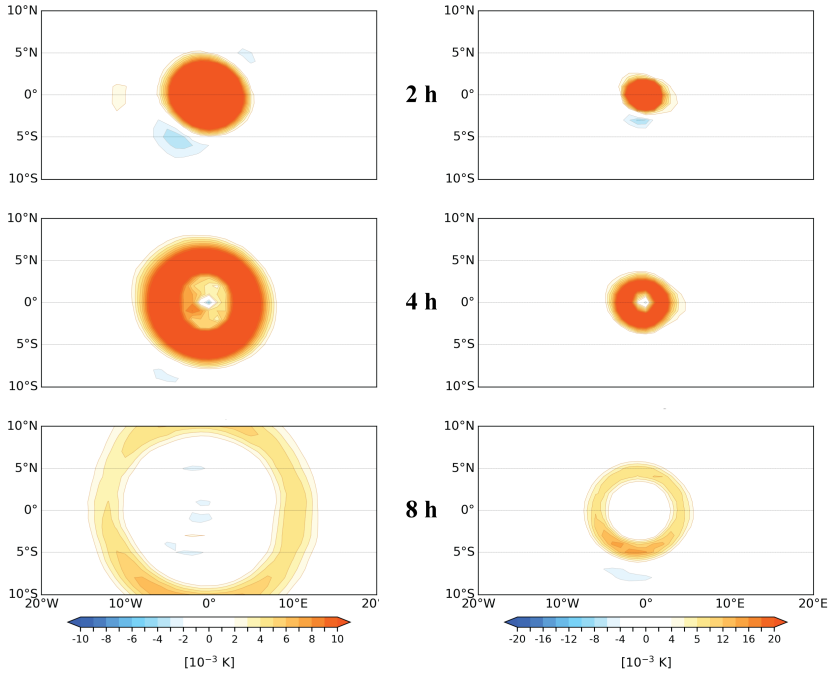

FIG. 9. Composites of high-pass filtered tropical tropospheric temperature constructed based on the top 10% of strongest downwelling events at individual referenced grid points along the equator, shown 2, 4, and 8 hours after the events, using hourly data for 2010-2019. (left) The reference timeseries is the average of the 700 and 300 hPa (geometric) vertical velocity, and the temperature field is represented by 1000-200 hPa thickness. (right) The reference timeseries is the difference of vertical velocity at 300 and 700 hPa, and the temperature field is represented by 500-200 hPa thickness.

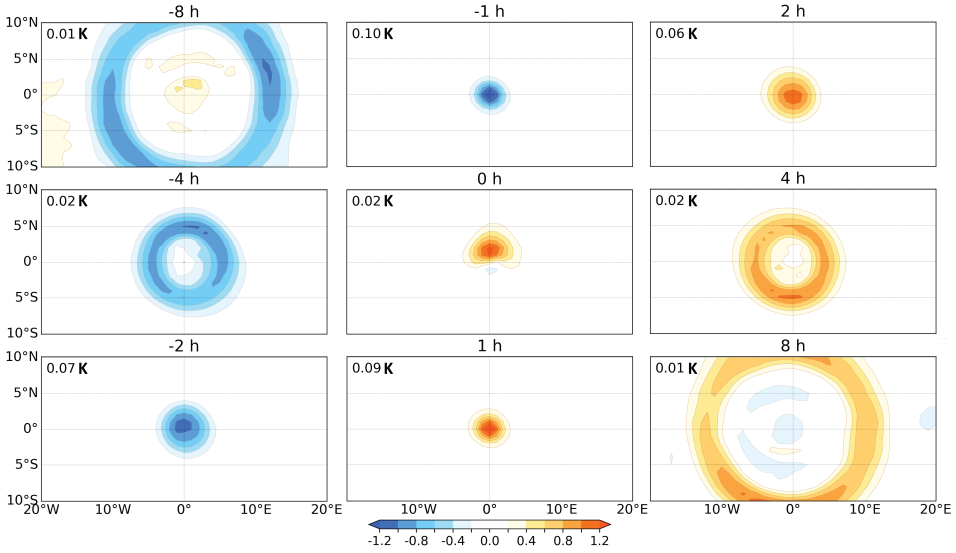

FIG. 10. The right panels are the same as those in the left panel of Fig. 9, but each panel is normalized relative to the average magnitude of the 1% of grids with strongest signal, which is given in the top left corner of each panel. The other panels show the composites at the other time lags as indicated.

be seen propagating towards the reference grid point (Fig. 10). Here we are using the strong downwelling events as a proxy for (unresolved) mesoscale updrafts in deep convection. Results based on the strongest upwelling events are discussed in Section 4.

Figure 10 also reveals that the strong downwelling events induce significant adiabatic warming when they arrive at the reference grid point at time zero. Note that the vertical velocity and temperature are in quadrature for the gravity waves. Consequently, the strongest downwelling corre-

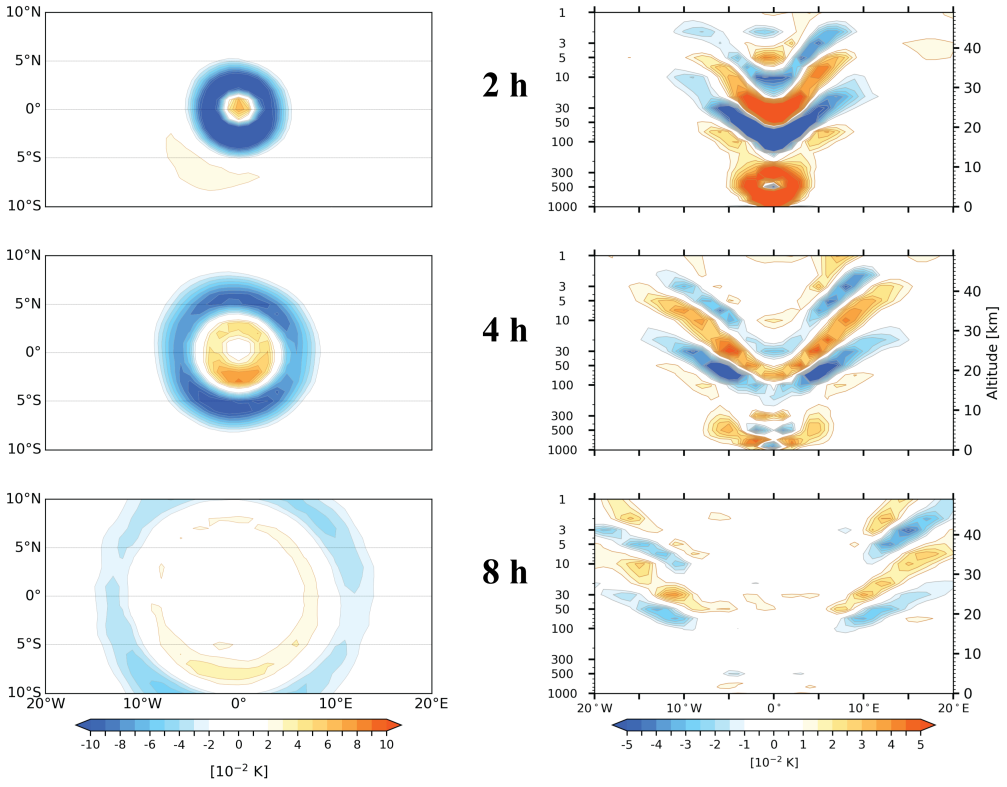

FIG. 11. Composites of high-pass filtered tropical temperature constructed based on the top 10% of strongest downwelling events at individual referenced grid points along the equator, shown 2, 4, and 8 hours after the events, using hourly data for 2010-2019. The reference timeseries is the average of the 700 and 300 hPa (geometric) vertical velocity. (left) Horizontal cross sections of temperature at the 50 hPa level. (right) The corresponding longitude-height cross sections of temperature along the equator.

sponds to the largest time rate of change of temperature, both of which occur at time zero. The lowest temperature at the reference grid point is observed an hour earlier and the highest temperature an hour later.

Figure 11 shows horizontal maps at the 50 hPa level (left), and the equatorial longitude-height sections (right) of temperature, composited based on the first mode, as represented by the average of w_{300} and w_{700}. The wave fronts radiate outward and upward relative to the respective reference grid points, and their amplitude decreases rapidly with time. The zonal cross sections show how gravity waves are refracted as they disperse upward from the troposphere into the stratosphere, due to the change in static stability at the tropopause, with the phase fronts assuming a V-shaped configuration (Lane et al. 2001). In the troposphere, the phase lines are oriented almost vertically, implying that the waves are trapped or evanescent or that the vertical wavelength is very long. Upon close inspection, it is evident from the zonal cross sections that the wave axes are propagating downward, while the group velocity and the vertical flux of mechanical energy is upward and outward. The zonal cross sections for temperature composited based on the second mode (i.e., the difference between w_{300} and w_{700}) are shown in Fig. S3. It is more difficult to capture the signal of the second mode based on compositing or regression analysis.

Figure 12 shows the corresponding structure in the wave-related fields in the three velocity components and geopotential at the 50 hPa level for the first mode, 8 hours after the strong downwelling events. It is evident that geopotential, geometric vertical velocity, and the radial wind component all vary in phase with each other, indicative of an upward flux of radial momentum and mechanical energy, consistent with the results of spectral analysis. There is a weak suggestion of an anticyclonic turning the horizontal wind vector, as in IG waves.

It can be seen from Figs. 9, 10, and 11 that the convectively generated gravity waves modify the troposphere by inducing adiabatic warming and cooling, and therefore, we might expect to see their signals in the other fields as well. Figure 13, which is constructed in the same manner as bottom left panel of Fig. 9, shows the gravity wave signatures in the cloud cover fraction, outgoing longwave radiation (OLR), and precipitation, and thus, documents the importance of gravity waves in modifying the state

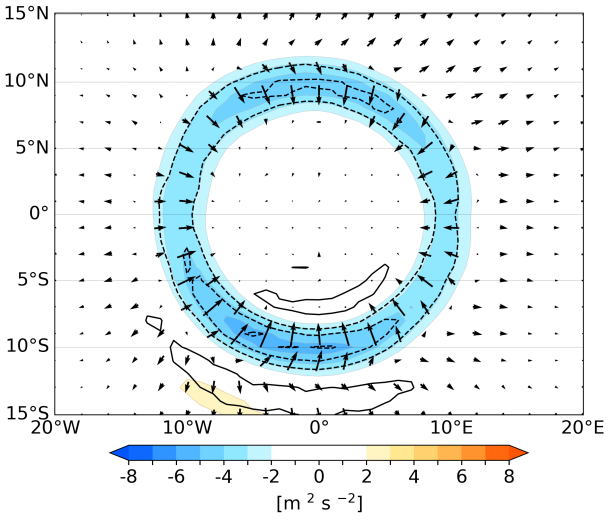

FIG. 12. Composite of high-pass filtered geopotential (colored shading), vertical velocity (positive upward, contour interval 0.4 mm s^{-1}, zero contour omitted, negative contours dashed), and horizontal winds (vectors, the longest correspond to 0.1 m s^{-1}) at the 50 hPa level based on top 10% of strongest downwelling events at individual referenced grid points along the equator, shown 8 hours after the reference time. The reference timeseries is the average of the 700 and 300 hPa (geometric) vertical velocity.

of the troposphere in addition to transporting energy and momentum upward into the stratosphere.

In the horizontal sections shown in Figs. 9-13, the meridional phase propagation is slightly stronger than the zonal propagation. A possible cause of this departure from circular symmetry is the greater variability of the zonal wind variations in the background flow, due in large part to the QBO in the stratosphere and the Madden-Julian oscillation (MJO) in the troposphere. Another contributing factor could be the fact that the patches of enhanced convection from which the waves emanate tend to be zonally elongated.

c. Seasonal dependence of gravity waves propagation

The composites shown in Fig. 14 are constructed in the same manner as those in the bottom left panel of Fig. 9, but separately for the 3-month seasons. It is readily apparent that the prevailing direction of wave propagation is northward in DJF and southward in JJA. The rings are more symmetric during the transition seasons, yet a slight preference for northward propagation is evident during MAM and for southward propagation during SON. These asymmetries in the direction of wave propagation relate to the distribution of wave sources relative to the reference grid points, which are located along the equator. When the prevailing component of the propagation is southward, as in JJA, we can infer that the wave sources should be located mainly to the north of the equator, and vice versa. This is indeed the case, as shown in Fig. 15, which shows the

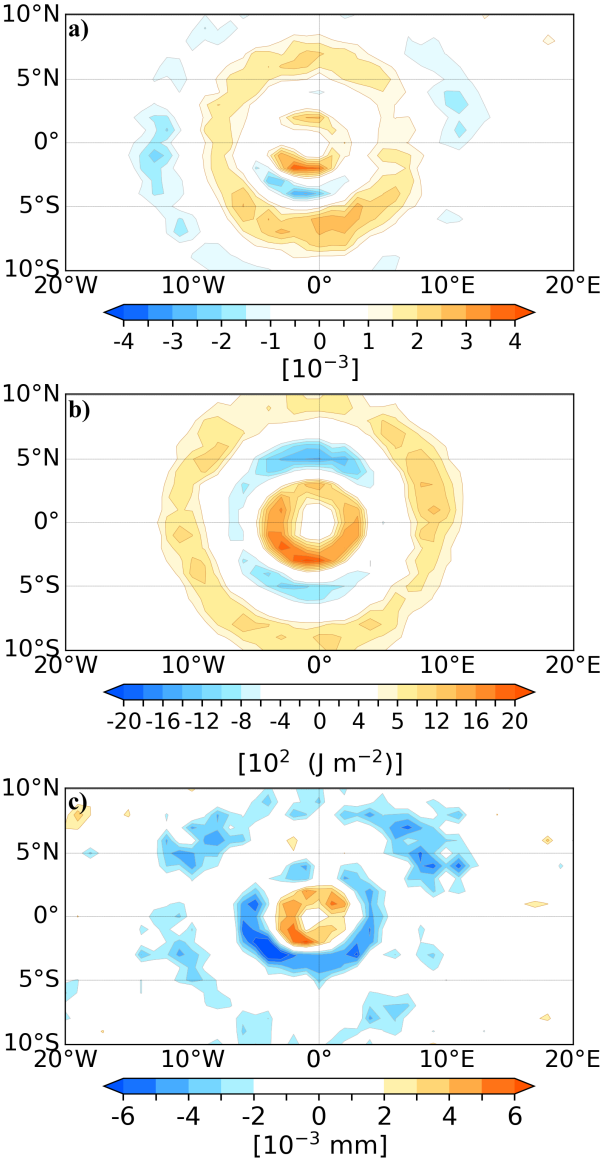

FIG. 13. Composite of high-pass filtered (a) total cloud fraction, (b) outgoing longwave radiation (OLR), and (c) precipitation based on top 10% of strongest downwelling events at individual referenced grid points along the equator, shown 8 hours after the reference time, using hourly data for 2010-2019. The reference timeseries is the average of the 700 and 300 hPa (geometric) vertical velocity. All the fields are from ERA5 data.

standard deviation of the unfiltered hourly vertical velocity field at the 50 hPa level, an indicator of wave activity. From this figure it can be inferred that the dominant regions of tropical wave activity correspond to the regions of strong convection, which are mostly located to the south of the equator during DJF and to the north of the equator during JJA. Tropical wave activity is significantly stronger during JJA than DJF (Fig. 15), and the southward component of wave propagation is more prevalent (Fig. 14). Other

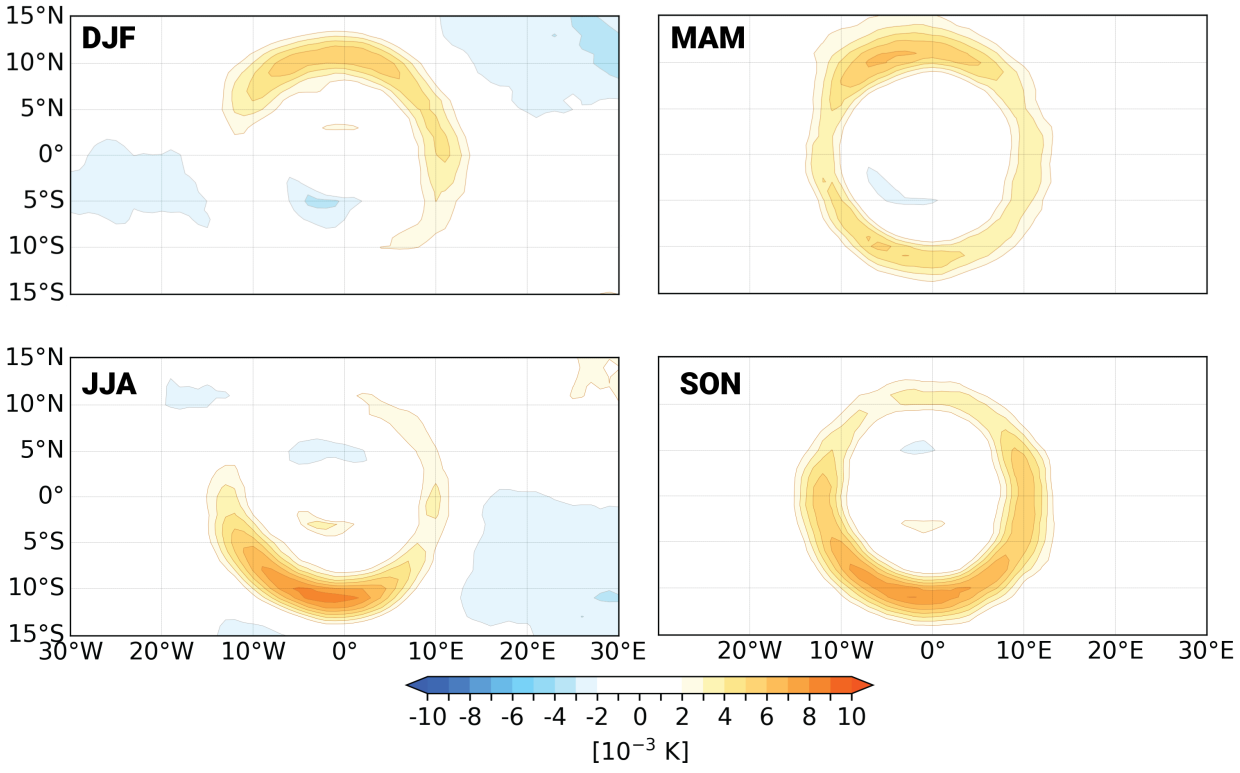

FIG. 14. As the bottom left panel of Fig. 9, but separated for four seasons.

notable features in Fig. 15 are the higher latitude, orographically induced waves and the enhanced wave activity along the extratropical storm tracks.

4. Discussion

Waves generated by convective heating are widely believed to have vertical wavelengths approximately twice the depth of the heating. This relationship, demonstrated by Garcia and Salby (1987) for large-scale waves, arises because the heating projects most strongly onto a wave with a vertical wavelength twice the depth of the heating. As the waves disperse upward from the troposphere into the stratosphere, they are refracted to half that vertical wavelength due to the twofold increase in buoyancy frequency at the tropopause. The frequency, and the horizontal, and vertical wavelengths of waves are then mutually related through the wave dispersion relationship. A simplified version of the dispersion relation for medium-frequency gravity waves can be written as:

$$\hat{c}_p = \frac{N\lambda_z}{2\pi} \tag{3}$$

where $\hat{c}_p$ is the intrinsic zonal phase speed, λ_z the vertical wavelength, and N the Brunt-Väisälä frequency, which is usually prescribed to be 0.022 s^{-1} at the stratospheric levels.Based on this equation (Fritts and Alexander 2003), the stratospheric vertical wavelength for waves with intrinsic phase speeds of 49 and 23 m s^{-1}, should be ~14 and ~6.5 km. Hence, we can expect that they should be generated by convective heating with depths of ~14 and ~6.5 km, respectively.

These wavelengths are consistent with the vertical scale of the first and second modes of the vertical profile of vertical velocity. Through the buoyancy force, the latent heating and vertical motion in the tropical troposphere are intrinsically coupled. It is also consistent with the vertical structure of the waves obtained by composite analysis and showed in Figs. 11 and S3. The first mode, which is associated with the heating profile in deep convection explains about half of the variance of tropical vertical velocity profile and the second mode, associated with shallow convection, explains another 20%.

Consistent with the literature, our results confirm the presence and preference of the first and second barocline modes, but we also see a broad continuum of gravity waves with a range of phase speeds centered around ±35 m s^{-1}. The presence of the other modes is bestillustrated by spectral analysis between two stratospheric levels, as shown in Fig. 16 for geopotential field between 10 and 50 hPa levels. Note that only the part of the spectrum with frequencies higher than 0.5 cpd is shown. The in-phase, out-of-phase,

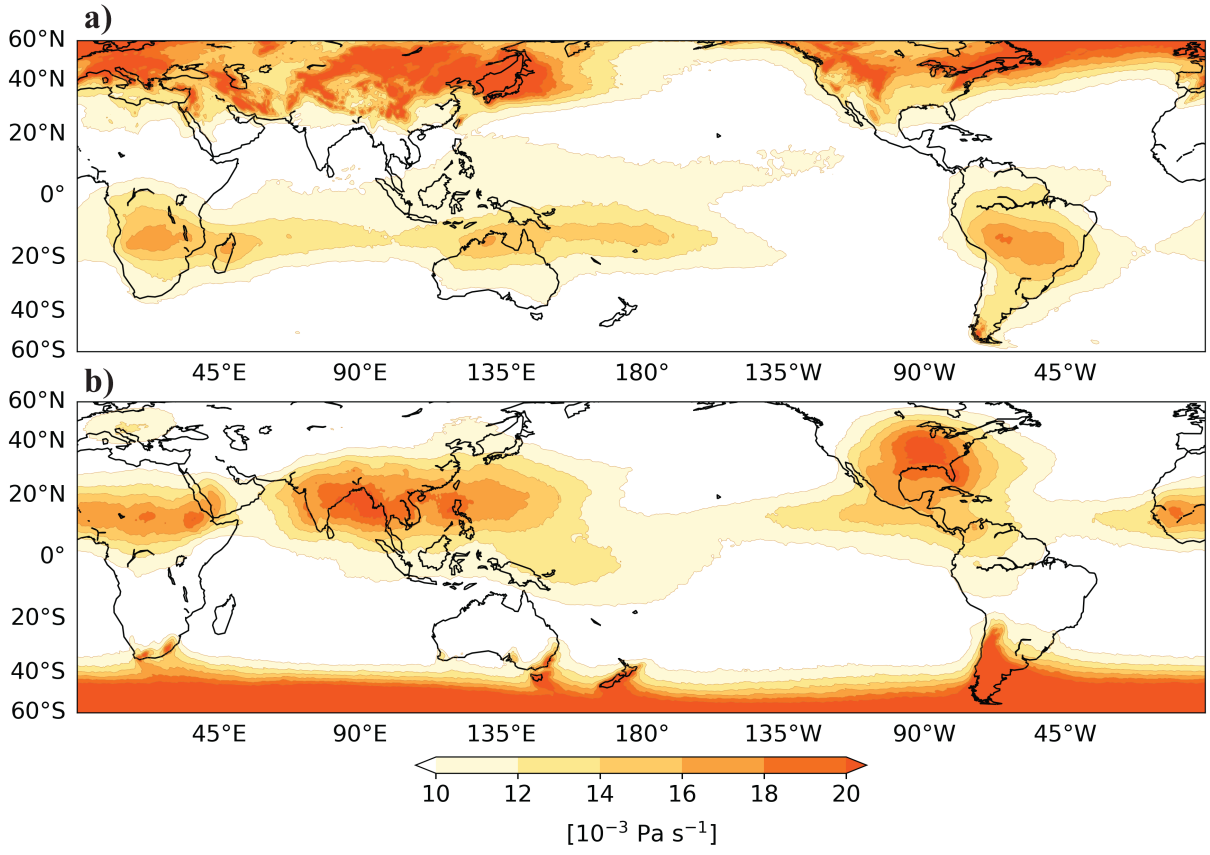

FIG. 15. Climatology of the standard deviation of vertical velocity at the 50 hPa level for (a) DJF, and (b) JJA, based on hourly data for 2010-2019.

or in-quadrature relationships along lines of constant phase speed are indicative of the presence of modal structures with well-defined vertical wavelengths. The exact relation depends on the vertical wavelength of a specific mode and the vertical distance between the two levels. For example, a wave with ~11 km vertical wavelength exhibits an in-phase relationship, because the distance between 10 and 50 hPa levels is ~11 km.

The coherence spectrum shown in Fig. 16c is a standardized measure of the strength of the linear relationship between the fluctuations in two variables (or the same variable at two different levels) that applies regardless of the phase difference between them. The coherence is strongest along and around the ±49 m s^{-1} phase speed lines. Bearing in mind that we are using a 10-year long record of hourly data along 180 meridians in computing these spectra gives us more than 27000 degrees of freedom, a coherence of ~0.03 is significant at the 99.9% level. If we consider only half of the meridians are statistically independent (the spatial autocorrelation of vertical velocity drops to zero at a distance of 3°), then a coherence of ~0.04 is 99.9% significant. By that measure, almost all the features we see in these cross spectra are highly statistically significant.

The compositing results presented in Figs. 9 to 14 are constructed based on downwelling events. Figure S4, which was constructed in the same manner as the left panels of Fig. 9, shows the corresponding patterns for upwelling events. The waves are of reversed polarity and only about half as strong as those associated with the downwelling events, even though the events that triggered them (i.e., the vertical velocity perturbations at time zero) are about 1.6 times as strong in absolute value. One possible explanation for this disparity is that there is some cancellation between the adiabatic cooling in wave-induced upwelling events and diabatic heating due to the release of latent heat in the deep convection. Since the deep convection is mostly unresolved in ERA5 reanalysis, the wave-induced adiabatic cooling is dominant, resulting in an anomalously colder temperature. Based on the results presented in Haertel and Kiladis (2004), if convection and its associated diabatic heating were fully resolved in ERA5, the degree of cancellation would be around 95% for the first mode, resulting in an even weaker temperature signature for the upwelling events.

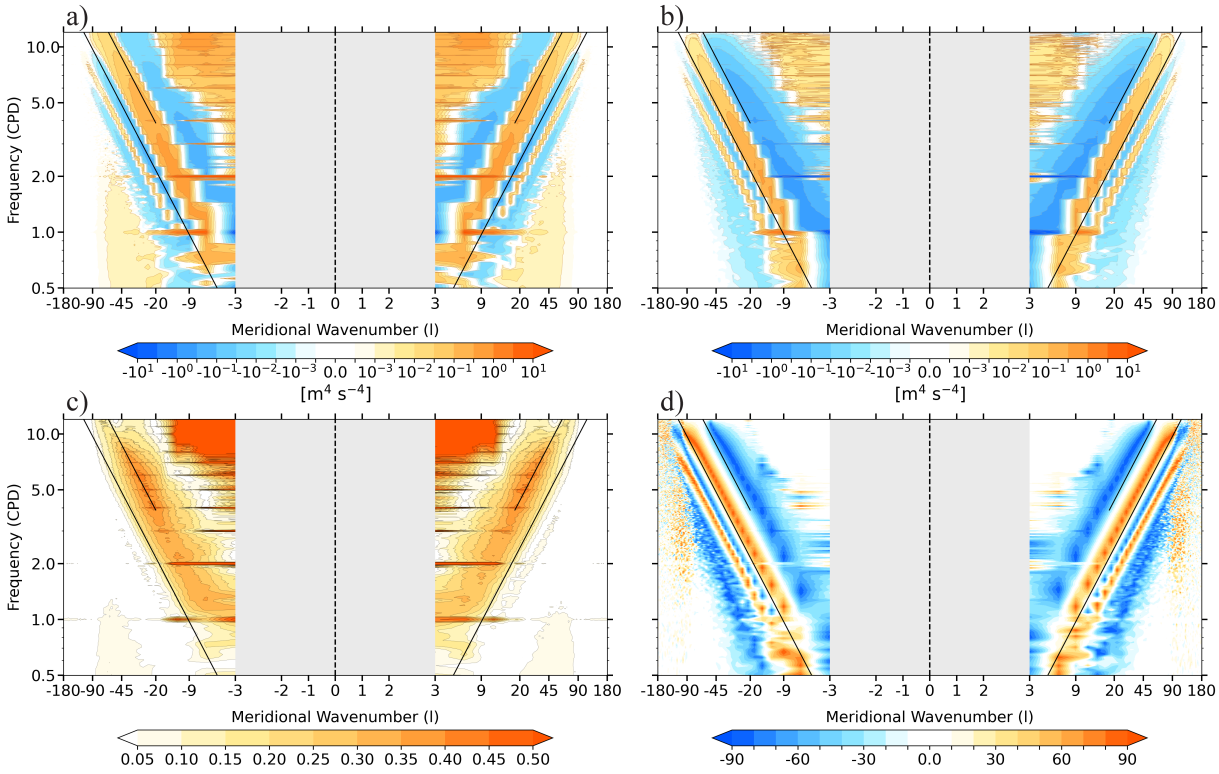

FIG. 16. Two-sided meridional wavenumber-frequency (a) cospectrum, (b) quadrature spectrum, (c) coherence spectrum, and (d) phase spectrum between geopotential field at the 10 and 50 hPa levels. The spectra are constructed in the same manner as Fig. 6 except that a Tukey window with α =0.33, which goes to zero at 30° S and 30° N, is applied to each meridian to mitigate the spectral leakage from high wavenumbers.

5. Concluding remarks

In this paper, we have investigated the characteristics of convectively generated gravity waves in the tropics using ERA5 reanalysis, and provided unique information on their spectrum, structure, and propagation in the atmosphere. Spectral analysis exhibited the signature of the gravity waves in a suite of atmospheric fields with phase speeds centered around ±35 m s^{-1} with preferred values around ±49 m s^{-1} and ±23 m s^{-1}, which correspond to the first and second baroclinic modes of diabatic heating, respectively. Compositing analysis revealed the three-dimensional structure of these waves and documented their signature in several atmospheric fields.

In this study, the gravity wave spectra presented at the 50 hPa level and compositing results at the stratospheric levels are based on a 10-year period (2010-2019), which includes both westerly and easterly phases of the QBO. The dependence of the properties of gravity waves upon the phase of the QBO is under investigation.

The ability of the ERA5 to resolve much of the broad spectrum of gravity waves opens avenues for further explorations in wave-driven variability of the general circulation. For instance, it provides a basis for investigating the wave-driven variability of the QBO period and amplitude, a topic that has previously been investigated only based on models. In Section 3.3 we only briefly discussed the seasonality of the tropical wave activity. It is evident from Fig. 15 that the strongest wave activity during JJA is north of 10°N, which is too far poleward to directly affect the QBO near the equator. How this spatiotemporal variability of wave activity modulates the stratospheric circulation, including the QBO characteristic can be studied using ERA5. It also provides a basis for investigating how the other dominant modes of the tropical variability including El Nino-Southern Oscillation (ENSO), and MJO modulate the tropical wave activity and hence influence the stratospheric circulation.

In the future, improved vertical and horizontal resolutions, and maybe specific data assimilation strategies, will enable NWP models to resolve an increased fraction of wave-induced variability, which will make them even more valuable than currently for wave-related studies.

Acknowledgments. This research is supported by the NASA Grant 80NSSC18K1031 and NSF Grant AGS-1821437. The authors declare no conflicts of interest.

Data availability statement. ERA5 hourly data was downloaded from the European Centre for Medium-Range Weather Forecasts (ECMWF), Copernicus Climate Change Service (C3S) at Climate Data Store (CDS, `https://cds.climate.copernicus.eu/`). The visible image shown in Fig. 1 is from `https://www.eorc.jaxa.jp/ptree/index.html`. The brightness temperature data shown in Fig. 1 are from `http://www.cr.chibau.jp/databases/GEO/H8_9/FD/index_jp.html`.

References

Alexander, M. J., and C. Barnet, 2007: Using Satellite Observations to Constrain Parameterizations of Gravity Wave Effects for Global Models. Journal of the Atmospheric Sciences, 64, 1652–1665, https://doi.org/10.1175/JAS3897.1.

Alexander, M. J., and D. A. Ortland, 2010: Equatorial waves in High Resolution Dynamics Limb Sounder (HIRDLS) data. Journal of Geophysical Research: Atmospheres, 115.

——, J. R. Holton, and D. R. Durran, 1995: The Gravity Wave Response above Deep Convection in a Squall Line Simulation. Journal of the Atmospheric Sciences, 52, 2212–2226, https://doi.org/10.1175/1520-0469(1995)052¡2212:TGWRAD¿2.0.CO;2.

Alexander, M. J., P. T. May, and J. H. Beres, 2004: Gravity waves generated by convection in the Darwin area during the Darwin Area Wave Experiment. Journal of Geophysical Research: Atmospheres, 109, https://doi.org/10.1029/2004JD004729.

Alexander, M. J., and Coauthors, 2010: Recent developments in gravity-wave effects in climate models and the global distribution of gravity-wave momentum flux from observations and models. Quarterly Journal of the Royal Meteorological Society, 136, 1103–1124, https://doi.org/10.1002/qj.637.

Bushell, A. C., and Coauthors, 2020: Evaluation of the Quasi-Biennial Oscillation in global climate models for the SPARC QBO-initiative. Quarterly Journal of the Royal Meteorological Society, n/a, https://doi.org/10.1002/qj.3765.

Butchart, N., J. A. Anstey, Y. Kawatani, S. M. Osprey, J. H. Richter, and T. Wu, 2020: QBO Changes in CMIP6 Climate Projections. Geophysical Research Letters, 47, e2019GL086903, https://doi.org/10.1029/2019GL086903.

Corcos, M., A. Hertzog, R. Plougonven, and A. Podglajen, Observation of gravity waves at the tropical Tropopause using superpressure balloons. Journal of Geophysical Research: Atmospheres, n/a, e2021JD035165, https://doi.org/10.1029/2021JD035165.

Dee, D. P., and Coauthors, 2011: The ERA-Interim reanalysis: configuration and performance of the data assimilation system. Quarterly Journal of the Royal Meteorological Society, 137, 553–597, https://doi.org/10.1002/qj.828.

Dunkerton, T. J., 1997: The role of gravity waves in the quasi-biennial oscillation. Journal of Geophysical Research: Atmospheres, 102, 26053–26076, https://doi.org/10.1029/96JD02999.

Ern, M., and Coauthors, 2014: Interaction of gravity waves with the QBO: A satellite perspective. Journal of Geophysical Research: Atmospheres, 119, 2329–2355.

Ern, M., Q. T. Trinh, P. Preusse, J. C. Gille, M. G. Mlynczak, J. M. Russell III, and M. Riese, 2018: GRACILE: a comprehensive climatology of atmospheric gravity wave parameters based on satellite limb soundings. Earth System Science Data, 10, 857–892, https://doi.org/10.5194/essd-10-857-2018.

Fritts, D. C., and M. J. Alexander, 2003: Gravity wave dynamics and effects in the middle atmosphere. Reviews of Geophysics, 41, https://doi.org/10.1029/2001RG000106.

Garcia, R. R., and M. L. Salby, 1987: Transient response to localized episodic heating in the tropics. Part II: Far-field behavior. Journal of the atmospheric sciences, 44, 499–532.

——, A. K. Smith, D. E. Kinnison, Á. de la Cámara, and D. J. Murphy, 2017: Modification of the Gravity Wave Parameterization in the Whole Atmosphere Community Climate Model: Motivation and Results. Journal of the Atmospheric Sciences, 74, 275–291, https://doi.org/10.1175/JAS-D-16-0104.1.

Geller, M. A., and Coauthors, 2013: A Comparison between Gravity Wave Momentum Fluxes in Observations and Climate Models. Journal of Climate, 26, 6383–6405, https://doi.org/10.1175/JCLI-D-12-00545.1.

Gupta, A., T. Birner, A. Dörnbrack, and I. Polichtchouk, 2021: Importance of Gravity Wave Forcing for Springtime Southern Polar Vortex Breakdown as Revealed by ERA5. Geophysical Research Letters, 48, e2021GL092762, https://doi.org/10.1029/2021GL092762.

Haertel, P. T., and G. N. Kiladis, 2004: Dynamics of 2-Day Equatorial Waves. Journal of the Atmospheric Sciences, 61, 2707–2721, https://doi.org/10.1175/JAS3352.1.

Haiden, T., and Coauthors, 2018: Use of in situ surface observations at ECMWF. https://doi.org/10.21957/dj9lpy4wa.

Hersbach, H., and Coauthors, 2020: The ERA5 global reanalysis. Quarterly Journal of the Royal Meteorological Society, 146, 1999–2049, https://doi.org/10.1002/qj.3803.

Hoffmann, L., and Coauthors, 2019: From ERA-Interim to ERA5: the considerable impact of ECMWF's next-generation reanalysis on Lagrangian transport simulations. Atmospheric Chemistry and Physics, 19, 3097–3124.

Holton, J. R., 1973: An Introduction to Dynamic Meteorology. American Journal of Physics, 41, 752–754, https://doi.org/10.1119/1.1987371.

Jewtoukoff, V., A. Hertzog, R. Plougonven, A. de la Cámara, and F. Lott, 2015: Comparison of gravity waves in the Southern Hemisphere derived from balloon observations and the ECMWF analyses. Journal of the Atmospheric Sciences, 72, 3449–3468.

Kawatani, Y., S. Watanabe, K. Sato, T. J. Dunkerton, S. Miyahara, and M. Takahashi, 2010: The Roles of Equatorial Trapped Waves and Internal Inertia–Gravity Waves in Driving the Quasi-Biennial Oscillation. Part I: Zonal Mean Wave Forcing. Journal of Atmospheric Sciences, 67, 963–980, https://doi.org/10.1175/2009JAS3222.1.

Kim, J.-E., and M. J. Alexander, 2015: Direct impacts of waves on tropical cold point tropopause temperature. Geophysical Research Letters, 42, 1584–1592, https://doi.org/10.1002/2014GL062737.

Lane, T. P., M. J. Reeder, and T. L. Clark, 2001: Numerical Modeling of Gravity Wave Generation by Deep Tropical Convection. Journal of the Atmospheric Sciences, 58, 1249–1274, https://doi.org/10.1175/1520-0469(2001)058¡1249:NMOGWG¿2.0.CO;2.

Matsuno, T., 1966: Quasi-Geostrophic Motions in the Equatorial Area. Journal of the Meteorological Society of Japan. Ser. II, 44, 25–43, https://doi.org/10.2151/jmsj1965.44.1-25.

Miller, S. D., W. C. Straka, J. Yue, S. M. Smith, M. J. Alexander, L. Hoffmann, M. Setvák, and P. T. Partain, 2015: Upper atmospheric gravity wave details revealed in nightglow satellite imagery. PNAS, 112, E6728–E6735, https://doi.org/10.1073/pnas.1508084112.

Nolan, D. S., and J. A. Zhang, 2017: Spiral gravity waves radiating from tropical cyclones. Geophysical Research Letters, 44, 3924–3931, https://doi.org/10.1002/2017GL073572.

Pahlavan, H. A., Q. Fu, J. M. Wallace, and G. N. Kiladis, 2021a: Revisiting the Quasi-Biennial Oscillation as Seen in ERA5. Part I: Description and Momentum Budget. Journal of the Atmospheric Sciences, 78, 673–691, https://doi.org/10.1175/JAS-D-20-0248.1.

——, J. M. Wallace, Q. Fu, and G. N. Kiladis, 2021b: Revisiting the Quasi-Biennial Oscillation as Seen in ERA5. Part II: Evaluation of Waves and Wave Forcing. Journal of the Atmospheric Sciences, 78, 693–707, https://doi.org/10.1175/JAS-D-20-0249.1.

Pautet, P.-D., M. J. Taylor, S. D. Eckermann, and N. Criddle, 2019: Regional Distribution of Mesospheric Small-Scale Gravity Waves During DEEPWAVE. Journal of Geophysical Research: Atmospheres, 124, 7069–7081, https://doi.org/10.1029/2019JD030271.

Piani, C., D. Durran, M. J. Alexander, and J. R. Holton, 2000: A Numerical Study of Three-Dimensional Gravity Waves Triggered by Deep Tropical Convection and Their Role in the Dynamics of the QBO. Journal of the Atmospheric Sciences, 57, 3689–3702, https://doi.org/10.1175/1520-0469(2000)057¡3689:ANSOTD¿2.0.CO;2.

Podglajen, A., A. Hertzog, R. Plougonven, and B. Legras, 2016: Lagrangian temperature and vertical velocity fluctuations due to gravity waves in the lower stratosphere. Geophysical Research Letters, 43, 3543–3553, https://doi.org/10.1002/2016GL068148.

——, ——, ——, and ——, 2020: Lagrangian gravity wave spectra in the lower stratosphere of current (re)analyses. Atmospheric Chemistry and Physics, 20, 9331–9350, https://doi.org/10.5194/acp-20-9331-2020.

Preusse, P., M. Ern, P. Bechtold, S. D. Eckermann, S. Kalisch, Q. T. Trinh, and M. Riese, 2014: Characteristics of gravity waves resolved by ECMWF. Atmospheric Chemistry and Physics, 14, 10483–10508, https://doi.org/10.5194/acp-14-10483-2014.

Rapp, M., and Coauthors, 2021: SOUTHTRAC-GW: An Airborne Field Campaign to Explore Gravity Wave Dynamics at the World's Strongest Hotspot. Bulletin of the American Meteorological Society, 102, E871–E893, https://doi.org/10.1175/BAMS-D-20-0034.1.

Richter, J. H., J. A. Anstey, N. Butchart, Y. Kawatani, G. A. Meehl, S. Osprey, and I. R. Simpson, 2020: Progress in Simulating the Quasi-Biennial Oscillation in CMIP Models. Journal of Geophysical Research: Atmospheres, 125, e2019JD032362, https://doi.org/10.1029/2019JD032362.

Sakazaki, T., and K. Hamilton, 2020: An Array of Ringing Global Free Modes Discovered in Tropical Surface Pressure Data. Journal of the Atmospheric Sciences, 77, 2519–2539, https://doi.org/10.1175/JAS-D-20-0053.1.

Schroeder, S., P. Preusse, M. Ern, and M. Riese, 2009: Gravity waves resolved in ECMWF and measured by SABER. Geophysical Research Letters, 36,

https://doi.org/10.1029/2008GL037054.

Shepherd, T. G., I. Polichtchouk, R. Hogan, and A. J. Simmons, 2018: Report on Stratosphere Task Force. https://doi.org/10.21957/0vkp0t1xx.

Skamarock, W. C., S.-H. Park, J. B. Klemp, and C. Snyder, 2014: Atmospheric kinetic energy spectra from global high-resolution nonhydrostatic simulations. Journal of the Atmospheric Sciences, 71, 4369–4381.

Song, I.-S., H.-Y. Chun, and T. P. Lane, 2003: Generation Mechanisms of Convectively Forced Internal Gravity Waves and Their Propagation to the Stratosphere. Journal of the Atmospheric Sciences, 60, 1960–1980, https://doi.org/10.1175/1520-0469(2003)060¡1960:GMOCFI¿2.0.CO;2.

Wright, C. J., N. P. Hindley, M. J. Alexander, L. A. Holt, and L. Hoffmann, 2021: Using vertical phase differences to better resolve 3D gravity wave structure. Atmospheric Measurement Techniques, 14, 5873–5886, https://doi.org/10.5194/amt-14-5873-2021.

Yamashita, C., H.-L. Liu, and X. Chu, 2010: Gravity wave variations during the 2009 stratospheric sudden warming as revealed by ECMWF-T799 and observations. Geophysical Research Letters, 37, https://doi.org/10.1029/2010GL045437.